
A symplectic analytical singular element for steady-state thermal conduction with singularities in anisotropic material

X.F. Hu^{a, b*}, W.A. Yao^{a, b}, S.T. Yang^c

^a *State Key Laboratory of Structural Analysis for Industrial Equipment, Dalian University of Technology, Dalian 116024, P. R. China*

^b *International Center for Computational Mechanics, Dalian University of Technology, Dalian, 116024, P. R. China.*

^c *Department of Civil and Environmental Engineering, University of Strathclyde, Glasgow, G1 1XJ, United Kingdom*

*Corresponding author: hxf@dlut.edu.cn

Abstract: Modelling of steady-state thermal conduction for crack and v-notch in anisotropic material remains challenging. Conventional numerical methods could bring significant error and the analytical solution should be used to improve the accuracy. In this study, crack and v-notch in anisotropic material are studied. The analytical symplectic eigen solutions are obtained for the first time and used to construct a new symplectic analytical singular element (SASE). The shape functions of the SASE are defined by the obtained eigen solutions (including higher order terms), hence the temperature as well as heat flux fields around the crack/notch tip can be described accurately. The formulation of the stiffness matrix of the SASE is then derived based on a variational principle with two kinds of variables. The nodal variable is transformed into temperature such that the proposed SASE can be connected with conventional finite elements directly without transition element. Structures of complex geometries and complicated boundary conditions can be analyzed numerically. The generalized flux intensity factors (GFIFs) can be calculated directly without any post-processing. A few numerical examples are worked out and it is proven that the proposed method is effective for the discussed problem, and the structure can be analyzed accurately and efficiently.

Keywords: Steady-state thermal conduction; anisotropic material; singular element; finite element method; numerical modelling

Nomenclature

$a^{(i)}$	the i th eigen expanding coefficients
a	crack length
A, B, C, D	coefficients in the general solution of eigenvector
\mathbf{A}, \mathbf{B}	diagonal matrix of eigenvalue
c	a non-zero constant
$d_{11}, d_{12}, d_{21}, d_{22}$	coefficients determined by D_{11}, D_{12}, D_{21} and D_{22}
$D_{11}, D_{12}, D_{21}, D_{22}$	equivalent thermal conductivity coefficients under the polar coordinate system
$\mathbf{f}_T, \mathbf{f}_r, \mathbf{f}_s$	vectors of the variables after separation of variable
\mathbf{H}	Hamiltonian operator matrix
$k_{11}, k_{12}, k_{21}, k_{22}$	thermal conductivity coefficients
k	$k = k_{11} = k_{12}$ for isotropic material
\mathbf{K}	stiffness matrix of the SASE
\mathbf{L}	transform matrix relates nodal temperature with expanding coefficient
N	number of sub-fields
P	number of nodes of the SASE
q_x, q_y	heat fluxes under the Cartesian coordinate system
q_r, q_θ	heat fluxes under the polar coordinate system
(r, θ)	global polar coordinate system
(r, ϑ)	local polar coordinate system
\mathbf{R}	matrix which relates eigenvectors of different sub-fields
S_r, S_θ	equivalent heat fluxes under the polar coordinate system
\mathbf{t}	vector of nodal temperature
T	temperature
T^*, S_r^*	temperature and heat flux fields in the SASE
T_c	constant
\mathbf{Z}	vector of the configuration variable and the dual variable
θ^*	opening angle of the wedge
ξ	$\xi = \ln r$
Δ	$\Delta = D_{12}^2 - D_{11}D_{22}$
$\Delta\theta$	opening angle of a sub-field
μ, Ψ	eigenvalue and eigenvector
Ψ_T, Ψ_r, Ψ_s	temperature and equivalent heat fluxes after separation of variable
$\Psi^{(0)}, \Psi^J$	eigenvector of zero eigenvalue and the corresponding Jordan form eigenvector
λ	eigenvalue introduced in solving the general solution of eigenvector
α, β	coefficients in the general solution of eigenvector
γ	vector of eigen expanding coefficients
Ω	coefficients in the expression of \mathbf{R}

1.Introduction

Smart material and structure such as functional graded materials (FGMs) have been widely used in engineering, most of which exhibit anisotropic heat conduction properties. Singularity problem may exist in these anisotropic materials due to sudden change of geometric topology, such as wedge and crack, which could possibly lead to crack propagation and catastrophic failure under thermal loading. To accurately predict the temperature and heat flux in the vicinity of a wedge tip in an anisotropic material, it is a very challenging task. However, this problem is of great practical importance and hence a reliable and effective numerical method would be desirable.

In analysis of heat conduction in anisotropic materials, the anisotropy has complicated the fundamental equations and the solving procedure is more difficult than the well-known isotropic material. A number of studies have been conducted but most of them did not consider the singularity problem due to the existence of wedge or crack [1, 2, 3, 4, 5, 6, 7, 8, 9, 10, 11, 12, 13]. Buroni *et al.*, studied three-dimensional (3D) steady-state heat conduction problem in anisotropic material. By using the “Radon” transform, the 3D problem was reduced to a two-dimensional (2D) problem, and the Green’s functions for heat vortex loops in full-space, half-space, and bimetals were derived [14]. Berger *et al.*, studied heat conduction in anisotropic inhomogeneous medium, and the Green’s function for a point source was obtained [15]. Shen *et al.* studied a 2D infinite body composed of three dissimilar bonded layers subjected to an arbitrary heat source, and an analytical solution was derived [16].

Analytical solution is very useful in understanding the temperature and heat flux distribution around the wedge tip and should be used in the development of numerical methods to improve the solving accuracy. However, in the analysis of thermal conduction problem of wedge in anisotropic material the equivalent heat conductivity coefficients become functions of θ under the polar coordinate system (r, θ) . Due to this reason, the symplectic approach proposed by some of the authors for the study of steady-state thermal conduction of crack in multiple isotropic materials [17, 18] cannot be applied directly to anisotropic materials. Actually, this problem also exists in other analytical methods, and special treatments must be adopted to obtain the analytical solution. The coordinate transformation technique which maps the original problem with some particular material symmetries into an equivalent isotropic one is a typical method [1, 2, 19]; but the boundary conditions are hard to handle by this method. Moreover, this kind of method becomes quite complex for multi-material problems[20]. Beside the coordinate transformation technique, other analytical methods were developed for the interested

problem. Hwu and Lee investigated the singularity order of heat flux of multi-bonded anisotropic wedges by using the Stroh formalism for plane anisotropic thermoelasticity, the general solutions were presented in a simple and compact form [21]. Chao and Chang studied the interface crack between two dissimilar anisotropic materials under uniform heat flux based on the Hilbert problem formulation, a special technique was used to determine the general solutions for thermal fields [22].

In practice, numerical methods are more useful than analytical methods for the modelling of the structure with complex geometric topology, loading condition or constrain type. However, conventional numerical methods may have significant error for the problem with singularity (due to existence of wedge or crack). Many advanced numerical methods have been proposed for modelling crack problems [23, 24, 25, 26]. Hosseini *et al.* demonstrated that the usage of crack tip enrichments in the extended finite element method (XFEM) could improve solving efficiency significantly in the investigation of functional graded materials under thermal and mechanical loading [27]. Yvonnet *et al.* employed 3D XFEM to model temperature jump across the material interface between two dissimilar materials to study the Kapitza thermal resistance [28]. Marin *et al.*, studied the singularity problem for 2D Helmholtz-type equations with meshless method and boundary element method (BEM) [29, 30, 31]. Mera *et al.*, studied steady-state heat conduction problem by using BEM, and it was demonstrated that the proposed method is accurate and stable [32, 33]. In recent years, the singular boundary method (SBM) was applied to the study of heat conduction problems in anisotropic material, non-homogeneous material, and the material with temperature-dependent thermal conductivities [34, 35, 36]. Shannon *et al.*, extended the quasidual function method (QDFM) for calculating the generalized edge flux intensity functions along circular singular edges, it was demonstrated that the proposed method possesses high accuracy and robustness [37]. The existing methods are either very complex [20] or just limited to find the singularity order [21]. The XFEM is very effective on modelling crack extension without remeshing, however, the implementation of the crack tip enrichment is very complex. Furthermore, the numerical predictions are proven to be sensitive to the integration points used in the crack tip elements [38]. Hence, numerical methods with high solving accuracy and efficiency should be developed.

In the previous studies on the steady-state thermal conduction problem for crack in isotropic materials, a kind of symplectic analytical singular finite element (SASE) was proposed [17, 18]. The temperature and thermal flux fields in the SASE were defined by the analytical eigen solution obtained by using the symplectic dual approach [39, 40, 41], and the finite element formulation was derived based on the variational principle. In the finite element (FE) modelling, the crack tip was occupied by

the SASE while the other area of the structure was meshed by using conventional elements. In this way, both of the singularity problem in the vicinity of the crack top and the complex geometry, loading condition and constrain types can be handled very well. It was demonstrated that the proposed numerical method which combines analytical eigen solution and conventional finite element method (FEM) together can bring substantial improvement on solving accuracy and efficiency compared with conventional FEM [17, 18]. However, as the equivalent conductivity coefficients are functions of θ for anisotropic material, the corresponding eigen solution cannot be solved due to the mathematical complexity. As such this problem has brought great challenges in extending the previous numerical method to anisotropic material.

In this study, the steady-state thermal conduction of a wedge in anisotropic material is investigated. The sub-field method is employed to divide the material around the wedge tip into several sub-fields (sectors), and the equivalent conductivity coefficients under the polar coordinate system in each sub-field are assumed to be constants. If the opening angle of each sector is small enough, the resulted error is considered to be negligible. The concept of sub-field method for solving anisotropic material has been employed by Li for searching the singularity order of wedge in 2D media and Reissner plate [42, 43], and by Hu for finding the singularity order of crack subject to antiplane shear loading [44]. Then, the symplectic dual approach is employed to solve the eigen solution for each sub-field. The local coordinate system is introduced for each sub-field to reduce the complexity of mathematical derivation and a chain-like relationship among the eigenvectors is built to express the general solution of the eigenvector in a simple and compact manner. The eigenvalue as well as eigenvector can be solved by the boundary conditions at the wedge surfaces. With the obtained eigen solution, a new SASE for steady-state thermal conduction of wedge in anisotropic material is constructed in the way similar to the previous studies [17, 18]. However, due to the changes of the fundamental equations, the derivation steps for eigenvalue as well as the formulation of the SASE are quite different from those reported in [17, 18]. By using the proposed SASE, the numerical prediction of the generalized flux intensity factors (GFIFs) can be solved directly without any post-processing. A few numerical examples have been worked out to demonstrate the proposed method, and to discuss other features such as the number of sub-fields, the number of Gaussian integration points in the calculation of the stiffness matrix, the size of the SASE, etc.

2. Fundamental equation

Consider the steady-state thermal conduction problem of a wedge with the opening angle θ^* ($\theta^*=2\pi$ for crack problem) in anisotropic material as shown in Fig.1. The heat fluxes q_x and q_y can be expressed in terms of temperature gradients under the Cartesian coordinate system as

$$\begin{bmatrix} q_x \\ q_y \end{bmatrix} = \begin{bmatrix} -k_{11} & -k_{12} \\ -k_{21} & -k_{22} \end{bmatrix} \begin{bmatrix} \frac{\partial T}{\partial x} \\ \frac{\partial T}{\partial y} \end{bmatrix} \quad (1)$$

where k_{11} , k_{22} , k_{12} and k_{21} are constant thermal conductivity coefficients and T is temperature. The conductivity coefficients are considered to obey the reciprocity relation[45]

$$k_{12} = k_{21} \quad (2)$$

Furthermore, according to irreversible thermodynamics, the coefficients k_{11} and k_{22} are positive. The magnitude of the coefficient k_{12} is limited by the requirement[45]

$$k_{11}k_{22} > k_{12}^2 \quad (3)$$

For isotropic material, the conductivity coefficients degenerate to $k = k_{11} = k_{22}$, $k_{12} = k_{21} = 0$.

The wedge problem considered here can be described under the polar coordinate system with the origin at the wedge tip O as shown in Fig.1. The heat flux components in the polar coordinate system can be obtained by using coordinate transformation, shown as follows,

$$\begin{bmatrix} q_r \\ q_\theta \end{bmatrix} = \begin{bmatrix} \cos \theta & \sin \theta \\ -\sin \theta & \cos \theta \end{bmatrix} \begin{bmatrix} q_x \\ q_y \end{bmatrix} \quad (4)$$

Similarly, the temperature gradients in the two coordinate systems have the following relationship:

$$\begin{bmatrix} \frac{\partial T}{\partial x} \\ \frac{\partial T}{\partial y} \end{bmatrix} = \begin{bmatrix} \cos \theta & -\sin \theta \\ \sin \theta & \cos \theta \end{bmatrix} \begin{bmatrix} \frac{\partial T}{\partial r} \\ \frac{1}{r} \frac{\partial T}{\partial \theta} \end{bmatrix} \quad (5)$$

Substituting Eqs.(1) and (5) into Eq.(4) gives the relationship between heat fluxes and temperature gradients under the polar coordinate system, as specified by

$$\begin{bmatrix} q_r \\ q_\theta \end{bmatrix} = \begin{bmatrix} D_{11} & D_{12} \\ D_{21} & D_{22} \end{bmatrix} \begin{bmatrix} \frac{\partial T}{\partial r} \\ \frac{1}{r} \frac{\partial T}{\partial \theta} \end{bmatrix} \quad (6)$$

where

$$D_{11} = -k_{11} \cos^2 \theta - 2k_{12} \sin \theta \cos \theta - k_{22} \sin^2 \theta \quad (7)$$

$$D_{12} = D_{21} = k_{12} (\sin^2 \theta - \cos^2 \theta) + (k_{11} - k_{22}) \sin \theta \cos \theta \quad (8)$$

$$D_{22} = -k_{11} \sin^2 \theta + 2k_{12} \sin \theta \cos \theta - k_{22} \cos^2 \theta \quad (9)$$

It is seen that D_{11} , D_{12} and D_{22} are equivalent conductivity coefficients under the polar coordinate system, and they are functions of θ for general anisotropic material. For isotropic material, these equivalent conductivity coefficients degenerate to $D_{11} = D_{22} = -k$, $D_{12} = 0$. However, the anisotropy has increased the mathematical complexity of the problem and the analytical solution become hard to find. Existing analytical methods use coordinate transformations which map the original problem into an equivalent isotropic one [19]. However, the solving procedures become very complex in treating the boundary conditions at the crack surfaces as well as multiple material crack/wedge problem. So, a simple and unified analytical approach must be developed.

There are three sets of typical boundary conditions at the wedge surfaces, as specified by

(1) prescribed heat flux

$$q_\theta|_{\theta=0 \text{ and } \theta^*} = 0 \quad (10)$$

(2) prescribed temperature

$$T|_{\theta=0 \text{ and } \theta^*} = 0 \quad (11)$$

(3) prescribed temperature and heat flux

$$T|_{\theta=0} = 0, \quad q_\theta|_{\theta=\theta^*} = 0 \text{ or } q_\theta|_{\theta=0} = 0, \quad T|_{\theta=\theta^*} = 0 \quad (12)$$

3. Sub-field method and local coordinate system

In this section, a sub-field method which divides the material around the wedge tip into several sub-fields (sectors) as shown in Fig.1 is used. Each sub-field occupies a sector which origins from the wedge tip, as illustrated in Fig.2. When sufficient numbers of sub-field are divided, the opening angle of each

sub-field is infinitely small, and the variation of D_{11} , D_{12} and D_{22} in each sub-field is negligible, or expressed as

$$(D_{11}(\theta_a), D_{12}(\theta_a), D_{22}(\theta_a)) \approx (D_{11}(\theta_b), D_{12}(\theta_b), D_{22}(\theta_b)), \text{ where } \theta_a, \theta_b \in [\theta_1, \theta_2] \quad (13)$$

where θ_a and θ_b are angular coordinates of two arbitrary points in a sub-field, and θ_1 and θ_2 represent the angular coordinates of the start and the end of a sub-field, respectively. Hence, the equivalent conductivity coefficients D_{11} , D_{12} and D_{22} can be assumed to be constants in each sub-field. The values of D_{11} , D_{12} and D_{22} should be calculated by Eqs.(7), (8) and (9). Theoretically, the angular coordinate of any point in the sub-field can be used in Eqs.(7), (8) and (9) for the calculation of D_{11} , D_{12} and D_{22} . Without loose of generality, we choose $\theta=(\theta_1 + \theta_2) / 2$ (the coordinate at the middle line of the sub-field) in the calculation.

It is expected that sufficient numbers of the sub-field should be divided in order to get an accurate prediction, and the mathematical derivation may be too complex as a result. In order to simplify the mathematical derivation, the local polar coordinate system is introduced for each sub-field, as shown in Fig.1. If the original wedge is divided into N ($N \geq 1$) sub-fields with the same sizes, then the opening angle of each sub-field is

$$\Delta\theta = \theta^* / N \quad (14)$$

The i th sub-field is described under the corresponding local polar coordinate system $OC_i\mathcal{G}_i$ with its origin at the wedge tip, and the angular coordinate always fall into the following range

$$0 < \mathcal{G}_i < \Delta\theta \quad (15)$$

The global polar coordinate system and the local coordinate system can be transformed into each other. For $\theta = \theta_0$ under the global polar coordinate system, the coordinate under the local coordinate system $OC_i\mathcal{G}_i$ is

$$\mathcal{G}(\theta_0) = \theta_0 - i \times \Delta\theta, \quad i = \text{round}(\theta_0 / \Delta\theta) \quad (16)$$

where the operator $\text{round}(x)$ rounds x to the nearest integer towards minus infinity. The two adjacent sub-fields are assumed to be perfectly bounded together, and the compatibility conditions at the “interface” can be specified by

$$T(\mathcal{G}_i = \Delta\theta) = T(\mathcal{G}_{i+1} = 0) \quad (17)$$

$$q_\theta(\mathcal{G}_i = \Delta\theta) = q_\theta(\mathcal{G}_{i+1} = 0) \quad (18)$$

It may be noted that the “interface” does not exist physically, it is artificially introduced in the proposed sub-field method. In the following discussions, the notation θ represents the global coordinate and \mathcal{G} represents the local coordinate system. The subscript of the local coordinate \mathcal{G}_i will be omitted hereinafter except where it may cause confusion for the sake of simplicity.

4.Symplectic dual equation

The equivalent conductivity coefficients are constants in each sub-field and the problem can be solved analytically by using the symplectic dual approach. Introduce the following transformations

$$\xi = \ln r, \quad S_r = rq_r, \quad S_\theta = rq_\theta \quad (19)$$

The fundamental equations under the polar coordinate system can be derived from the following equation of dissipation of quantity of heat as specified by

$$\sum_{i=1}^N \delta \int_0^{\Delta\theta} \int_0^\infty \left[S_{r,i} \frac{\partial T_i}{\partial \xi} + S_{\theta,i} \frac{\partial T_i}{\partial \mathcal{G}_i} - \frac{1}{2} (d_{11,i} S_{r,i}^2 + 2d_{12,i} S_{r,i} S_{\theta,i} + d_{22,i} S_{\theta,i}^2) \right] d\xi d\mathcal{G}_i = 0 \quad (20)$$

where

$$\begin{bmatrix} d_{11} & d_{12} \\ d_{21} & d_{22} \end{bmatrix} = \begin{bmatrix} D_{11} & D_{12} \\ D_{21} & D_{22} \end{bmatrix}^{-1} \quad (21)$$

is used to simplify the notation. Making the variation of Eq.(20) with respect to S_θ , the following relationship can be obtained

$$S_\theta = D_{12} r \frac{\partial T}{\partial r} + D_{22} \frac{\partial T}{\partial \mathcal{G}} \quad (22)$$

Substitute S_θ back into Eq.(20), the variational principle can be transformed into

$$\sum_{i=1}^N \delta \int_0^{\Delta\theta} \int_0^\infty \left[S_{r,i} \frac{\partial T_i}{\partial \xi} + \frac{1}{2d_{22,i}} \left(\frac{\partial T_i}{\partial \mathcal{G}_i} \right)^2 - \frac{d_{12,i}}{d_{22,i}} S_{r,i} \frac{\partial T_i}{\partial \mathcal{G}_i} + \frac{d_{12,i}^2 - d_{11,i} d_{22,i}}{2d_{22,i}} S_{r,i}^2 \right] d\xi d\mathcal{G}_i = 0 \quad (23)$$

Here T is also known as the configuration variable while S_r is the dual variable. Make the variations with respect to T and S_r respectively, the symplectic dual equation can be determined and specified by

$$\dot{\mathbf{Z}} = \mathbf{HZ} \quad (24)$$

where

$$\mathbf{H} = \begin{bmatrix} -\frac{D_{12}}{D_{11}} \frac{\partial}{\partial \mathcal{G}} & \frac{1}{D_{11}} \\ \frac{\Delta}{D_{11}} \frac{\partial^2}{\partial \mathcal{G}^2} & -\frac{D_{12}}{D_{11}} \frac{\partial}{\partial \mathcal{G}} \end{bmatrix} \text{ and } \Delta = D_{12}^2 - D_{11}D_{22} \quad (25)$$

In Eq.(24), $\mathbf{Z} = [T, S_r]^\top$ is the vector of configuration variable and the dual variable, and the dot represents differentiation with respect to ξ . \mathbf{H} is a Hamiltonian operator matrix. Unlike conventional analytical method which transforms the original problem into a higher order partial differential equation, the symplectic dual equation is a first order differential equation set which can be solved by using the method of separation of variables. Write the vector \mathbf{Z} in the form of

$$\mathbf{Z} = \exp(\xi\mu)\boldsymbol{\psi}(\mathcal{G}), \text{ where } \boldsymbol{\psi}(\mathcal{G}) = [\psi_T(\mathcal{G}), \psi_r(\mathcal{G})]^\top \quad (26)$$

where μ is the eigenvalue and $\boldsymbol{\psi}$ is the corresponding eigenvector, they form an eigen pair. The components of the eigenvector are temperature T and equivalent heat flux S_r after separation of variable, respectively. Similarly, $\psi_s(\mathcal{G})$ is used to denote S_θ after separation of variable and this notation will be used in the future discussions. Substitute \mathbf{Z} back into Eq.(24), the characteristic equation can be obtained and specified by

$$\mathbf{H}\boldsymbol{\psi} = \mu\boldsymbol{\psi} \quad (27)$$

The characteristic equation (27) can be solved analytically and the eigen solution are specified in the next section.

The typical boundary conditions represented by the new notations are specified by

(1) prescribed heat flux

$$\psi_s(\mathcal{G})|_{\theta=0 \text{ and } \theta^*} = 0 \quad (28)$$

(2) prescribed temperature

$$\psi_T(\mathcal{G})|_{\theta=0 \text{ and } \theta^*} = 0 \quad (29)$$

(3) prescribed temperature and heat flux

$$\psi_T(\mathcal{G})|_{\theta=0} = 0, \psi_s(\mathcal{G})|_{\theta=\theta^*} = 0 \text{ or } \psi_s(\mathcal{G})|_{\theta=0} = 0, \psi_T(\mathcal{G})|_{\theta=\theta^*} = 0 \quad (30)$$

The coordinates in the above boundary conditions are given in the global coordinate system, and they should be converted into local coordinate system through Eq.(16) in practice.

5. Eigen solution

5.1. Eigenvector corresponding to zero eigenvalue

Zero eigenvalue ($\mu = 0$) is a special case and should be discussed separately. If $\mu = 0$ then the characteristic equation (27) is simplified into

$$\mathbf{H}\boldsymbol{\psi} = 0 \quad (31)$$

Solving procedure of the above equation is straightforward and therefore is not presented in this paper. The results are summarized as follows:

- (1) For prescribed temperature boundary condition defined in Eq.(11), zero eigenvalue does not exist.
- (2) For mixed boundary condition defined in Eq.(12), zero eigenvalue does not exist.
- (3) For prescribed heat flux boundary condition defined in Eq.(10), zero eigenvalue exist and the corresponding eigenvector is specified by

$$\boldsymbol{\psi}^{(0)} = [1, 0]^T \quad (32)$$

It represents constant temperature without heat source in the domain. And Jordan form eigen solution should be solved through the following equation

$$\mathbf{H}\boldsymbol{\psi}^J = \boldsymbol{\psi}^{(0)} \quad (33)$$

The explicit form of the Jordan form eigenvector is specified by

$$\boldsymbol{\psi}^J = \left[-\frac{D_{12}}{D_{22}} \vartheta + T_c \quad D_{11} - \frac{D_{12}^2}{D_{22}} \right]^T \quad (34)$$

where T_c is a constant which should be determined by the compatibility condition defined in Eqs.(17) and (18). The solution to the original problem corresponding to the Jordan form eigenvector should be constructed through:

$$\mathbf{Z}^J = \boldsymbol{\psi}^J + \xi \boldsymbol{\psi}_0 = \left[-\frac{D_{12}}{D_{22}} \vartheta + T_c + \xi \quad D_{11} - \frac{D_{12}^2}{D_{22}} \right]^T \quad (35)$$

The Jordan form eigen solution represents a center heat generation which is not considered in this study, while it is introduced here for the completeness of the eigen solution.

5.2. General solution of eigenvector corresponding to nonzero eigenvalue

For nonzero eigenvalue and the corresponding eigenvector, Eq.(27) should be solved. The characteristic equation of Eq. (27) can be specified as follows

$$D_{22}\lambda^2 + 2D_{12}\lambda\mu + D_{11}\mu^2 = 0 \quad (36)$$

where λ is the eigenvalue of Eq. (27). The roots of the above equation are specified by

$$\lambda = \alpha \pm \beta, \text{ where } \alpha = -\frac{D_{12}}{D_{22}}\mu, \beta = \frac{\sqrt{\Delta}}{D_{22}}\mu \quad (37)$$

Hence, the general solution of $\psi(\mathcal{G})$ is specified by

$$\psi(\mathcal{G}) = \exp(\alpha\mathcal{G}) \begin{bmatrix} A \cosh(\beta\mathcal{G}) + B \sinh(\beta\mathcal{G}) \\ C \cosh(\beta\mathcal{G}) + D \sinh(\beta\mathcal{G}) \end{bmatrix} \quad (38)$$

The four coefficients are not independent, substitute it into Eq.(27) gives

$$C = (D_{11}\mu + D_{12}\alpha)A + D_{12}\beta B \quad (39)$$

$$D = D_{12}\beta A + (D_{11}\mu + D_{12}\alpha)B \quad (40)$$

Hence, the general solution is transformed into

$$\psi(\mathcal{G}) = \exp(\alpha\mathcal{G}) \begin{bmatrix} \cosh(\beta\mathcal{G}) & \sinh(\beta\mathcal{G}) \\ (D_{11}\mu + D_{12}\alpha)\cosh(\beta\mathcal{G}) + D_{12}\beta\sinh(\beta\mathcal{G}) & D_{12}\beta\cosh(\beta\mathcal{G}) + (D_{11}\mu + D_{12}\alpha)\sinh(\beta\mathcal{G}) \end{bmatrix} \begin{bmatrix} A \\ B \end{bmatrix} \quad (41)$$

and

$$\psi_s(\mathcal{G}) = D_{22}\beta \exp(\alpha\mathcal{G}) [A \sinh(\beta\mathcal{G}) + B \cosh(\beta\mathcal{G})] \quad (42)$$

From Eqs.(41) and (42), it is clear that only the coefficients A and B are unknown. The explicit form of the eigenvector can be specified once A and B are obtained. The eigen solution in different sub-fields are not independent on each other, while they should be related through the compatibility condition at the material interface defined in Eqs.(17) and (18). Therefore the relationship between two eigenvectors in the adjacent sub-fields is specified by

$$\begin{bmatrix} A_{n+1} \\ B_{n+1} \end{bmatrix} = \mathbf{R}_n \begin{bmatrix} A_n \\ B_n \end{bmatrix} \quad (43)$$

where

$$\mathbf{R}_n = e^{\alpha_n \Delta \theta} \begin{bmatrix} \cosh(\beta_n \Delta \theta) & \sinh(\beta_n \Delta \theta) \\ \Omega_n \sinh(\beta_n \Delta \theta) & \Omega_n \cosh(\beta_n \Delta \theta) \end{bmatrix} \Omega_n = \frac{D_{22,n} \beta_n}{D_{22,n+1} \beta_{n+1}}, \quad n = 1, 2, 3, \dots, N-1 \quad (44)$$

The subscript " n " represents n th sub-field. In addition, the coefficients of any sub-field can be expressed by these of the first sub-field as

$$\begin{bmatrix} A_n \\ B_n \end{bmatrix} = \prod_{i=1}^n \mathbf{R}_i \begin{bmatrix} A_1 \\ B_1 \end{bmatrix} \quad (45)$$

The eigenvalue and the coefficients A and B in the eigenvector should be determined by the boundary conditions at the wedge surfaces, as defined in Eqs.(10), (11) and (12). Actually, the coefficients A and B are determined by the boundary condition at $\theta=0$, and the eigenvalue is determined by the boundary condition at $\theta=\theta^*$.

5.3.Determination of the coefficients A and B

(1) for prescribed heat flux at $\theta=0$, substituting $\mathcal{G}=0$ into the solution of the first sub-field gives

$$B_1 = 0 \quad (46)$$

Therefore, a non-trivial solution of A and B is

$$A_1 = 1, B_1 = 0 \quad (47)$$

(2)for prescribed temperature at $\theta=0$, substituting $\mathcal{G}=0$ into the solution of the first sub-field returns

$$A_1 = 0 \quad (48)$$

Therefore, a non-trivial solution of A and B is

$$A_1=0, B_1 = 1 \quad (49)$$

5.4.Governing equation of nonzero eigenvalue

(1) for prescribed heat flux at $\theta=\theta^*$, substituting $\mathcal{G}=\Delta\theta$ into the solution of the last sub-field gives

$$\left[\sinh(\beta\Delta\theta) \quad \cosh(\beta\Delta\theta) \right] \prod_{i=n-1}^1 \mathbf{R}_i \begin{bmatrix} A_1 \\ B_1 \end{bmatrix} = 0 \quad (50)$$

(2)for prescribed temperature at $\theta=\theta^*$, substituting $\mathcal{G}=\Delta\theta$ into the solution of the last sub-field gives

$$\left[\cosh(\beta\Delta\theta) \quad \sinh(\beta\Delta\theta) \right] \prod_{i=n-1}^1 \mathbf{R}_i \begin{bmatrix} A_1 \\ B_1 \end{bmatrix} = 0 \quad (51)$$

The only unknown in Eqs.(50) and (51) for different boundary conditions is the eigenvalue μ which can be solved directly. The values of A_1 and B_1 have been obtained for different boundary conditions and specified in Eqs.(47) and (49). As such, all possible combinations of the boundary conditions have been considered and the eigen pairs can be solved. However, analytical approach cannot be used due to the mathematical complexity, numerical method such as Newton iteration method should be used to find the eigenvalues. Once the eigenvalues are obtained, the explicit forms of the eigenvector corresponding to each eigenvalue are obtained.

5.5. Eigen expansion

When the eigen solutions are obtained, the solution of the original problem can be expressed in the form of eigen expansion

$$\mathbf{Z} = \sum_{i=0}^{\infty} a^{(i)} \exp(\xi\mu^{(i)}) \boldsymbol{\psi}^{(i)}(\vartheta) \quad (52)$$

where the superscript i represents the i th expanding term, and $i=0$ represents the eigen solution of zero eigenvalue. It is noted that the Jordan form which represents a center heat source in the wedge tip is not considered in this study and hence it is not included in the eigen expansion. $a^{(i)}$ is the unknown expanding coefficients and should be determined. The temperature and heat flux field around the wedge tip are known explicitly once all the expanding coefficients are obtained. Here the eigenvector $\boldsymbol{\psi}(\vartheta)$ is a piece wise function and should be calculated separately. It may be noted that the values of the material properties in each sub-field are different and also should be calculated separately.

6. Symplectic Analytical Singular Element (SASE)

Due to the singular heat flux field around the vicinity of the wedge tip, conventional FEM may bring significant error. This study proposes a new element for steady-state thermal conduction problem of wedge in anisotropic material as shown in Fig.3. The node index is arranged from 1 to P , and the number of nodes P is not limited to a specific value; more nodes will favor the solving accuracy. The area around the wedge tip is meshed by the proposed element while the other area of the structure is occupied by conventional finite elements.

6.1. Shape function

Choosing the first P terms from Eq.(52) as trial functions, the temperature and heat flux in the proposed element can be expressed in the form of matrix as follows

$$T^* = \mathbf{f}_T^T \mathbf{A} \boldsymbol{\gamma}, \quad S_r^* = \mathbf{f}_r^T \mathbf{A} \boldsymbol{\gamma} \quad (53)$$

where $\boldsymbol{\gamma}$ is the vector of the expanding coefficients, as specified by

$$\boldsymbol{\gamma} = [a^{(0)}, a^{(1)}, a^{(2)}, \dots]^T \quad (54)$$

And \mathbf{A} is a diagonal matrix of which the components are formed by eigenvalues, it is given by

$$\mathbf{A} = \text{diag}(e^{\xi\mu^{(0)}}, e^{\xi\mu^{(1)}}, e^{\xi\mu^{(2)}} \dots) \quad (55)$$

The vectors \mathbf{f}_T and \mathbf{f}_r are formed by the components in the eigenvector, as specified by

$$\mathbf{f}_T = [\psi_T^{(0)}, \psi_T^{(1)}, \dots, \psi_T^{(P)}]^T, \quad \mathbf{f}_r = [\psi_r^{(0)}, \psi_r^{(1)}, \dots, \psi_r^{(P)}]^T \quad (56)$$

The only unknowns are the expanding coefficients in shape functions defined in Eq.(53), however, it is more acceptable to use nodal temperature as the unknowns in the shape function. Moreover, transition element must be involved to connect the proposed element with the surrounding conventional element if the expanding coefficients are used as the unknowns in the shape function. Hence, the shape function defined in Eq.(53) must be modified to take nodal temperature as the unknowns. Substituting the coordinates of the i -th node (ρ, θ_i) into Eq.(53), the nodal temperature vector $\mathbf{t} = [T_1, T_2, \dots, T_p]^T$ can be represented by the vector $\boldsymbol{\gamma}$, as specified by

$$\mathbf{t} = \mathbf{L}\boldsymbol{\gamma} \quad (57)$$

where $\mathbf{B} = \text{diag}(e^{\mu^{(0)} \ln \rho}, e^{\mu^{(1)} \ln \rho}, e^{\mu^{(2)} \ln \rho}, \dots)$ and \mathbf{L} is the transform matrix specified by

$$\mathbf{L} = \begin{bmatrix} \psi_T^{(0)}(\theta_1), \psi_T^{(1)}(\theta_1), \dots, \psi_T^{(P)}(\theta_1) \\ \psi_T^{(0)}(\theta_2), \psi_T^{(1)}(\theta_2), \dots, \psi_T^{(P)}(\theta_2) \\ \dots \\ \psi_T^{(0)}(\theta_p), \psi_T^{(1)}(\theta_p), \dots, \psi_T^{(P)}(\theta_p) \end{bmatrix} \quad (58)$$

In fact, the matrix \mathbf{B} is obtained by substituting the radial coordinate of the nodes ($\xi = \ln \rho$) into Eq.(55) and each line of the matrix \mathbf{L} is the vector \mathbf{f}_T defined in Eq.(56) with θ be the nodal angular coordinate. Here the angular coordinates are given under the global coordinate for the sake of simplicity, and in the implementation of codes the local coordinate which can be calculated through Eq.(16) is used.

According to Eq.(57), the vector of expanding coefficients $\boldsymbol{\gamma}$ can be expressed by the vector of nodal temperature, as specified by

$$\boldsymbol{\gamma} = \mathbf{B}^{-1}\mathbf{L}^{-1}\mathbf{t} \quad (59)$$

In order to get the inverse of matrix \mathbf{L} , it is required that \mathbf{L} is a square matrix. It means that the number of nodes is equal to the number of expanding terms in Eq.(56). Substitute $\boldsymbol{\gamma}$ back into Eq.(53), the temperature and equivalent heat flux are transformed into

$$\mathbf{T}^* = \mathbf{f}_T^T \mathbf{A} \mathbf{B}^{-1} \mathbf{L}^{-1} \mathbf{t}, \quad \mathbf{S}_r^* = \mathbf{f}_r^T \mathbf{A} \mathbf{B}^{-1} \mathbf{L}^{-1} \mathbf{t} \quad (60)$$

So far the only unknowns are the nodal temperature, and thus the present element can be connected to conventional temperature mode based elements directly without any transition element. Instead of using regular polynomials, the proposed new element employs the analytical eigen solutions to define the interior temperature and heat flux fields. At least two advantages have been introduced by this method,

i.e., (1) the heat flux singularity (singularity order and the angular distribution of heat fluxes) at the wedge tip in anisotropic material has been included in the heat flux field; and (2) the heat fluxes in the new element have the same accuracy order as temperature, and the solving accuracy of the proposed numerical method can be ensured.

6.2. Stiffness matrix

Substitute T^* and S_r^* back into the variational principle specified in Eq.(23) and notice that the trial functions have satisfied all the fundamental equations as well as the boundary conditions at the wedge surfaces, the variational principle in Eq.(23) can be transformed into

$$\delta \left\{ \sum_{i=1}^N \int_0^{\Delta\theta} [T_i^* S_{r,i}^*]_{\xi=\ln\rho} d\vartheta_i \right\} = 0 \quad (61)$$

In addition, the stiffness matrix can be obtained directly and specified by

$$\mathbf{K} = \mathbf{L}^{-T} \left(\sum_{i=1}^N \int_0^{\Delta\theta} \mathbf{f}_T \mathbf{f}_r^T d\vartheta_i \right) \mathbf{L}^{-1} \quad (62)$$

The interior fields of the developed element are described by using the above obtained analytical symplectic eigen solutions, for this reason it is termed as ‘‘symplectic analytical singular element (SASE)’’. It can be seen that the stiffness matrix is independent on the size of the SASE ρ , it this special feature is very useful in ensuring the accuracy and stability of the element.

7. Generalized flux intensity factors (GFIFs)

Assemble the stiffness matrix of the SASE into the global stiffness matrix and solve the global equation, the vector of nodal temperature \mathbf{t} of the proposed SASE can be extruded directly. Additionally the expanding coefficients in the vector \mathcal{Y} can be solved directly without any post processing through Eq.(59). In Ref.[19], the eigen expanding coefficients $a^{(i)}$ ($i=0,1,2,\dots$) are termed as generalized flux intensity factors (GFIFs), and such a definition is adopted in this study. The solving procedure is illustrated in Fig.4. The stiffness matrix of the SASE should be integrated over each sub-field separately; this is due to the variation of material properties in different sub-fields. In each sub-field, the integration can be conducted numerically, and Gaussian integration method is used in this study. The proposed symplectic dual approach and the SASE for anisotropic material are implemented with MATLAB code.

8. Numerical examples

8.1. Eigenvalues of a crack in anisotropic material

Consider a crack in an anisotropic material of which the conductivity properties are specified by $k_{11} = -1$, $k_{22} = -2$ and $k_{12} = 0.75$. Prescribed heat flux boundary condition at both of the crack surfaces defined in Eq.(10) is considered. Analytical solution of eigenvalue [19] exists and is specified as follows

$$\mu = \frac{n}{2}, n = 0, \pm 1, \pm 2 \quad (63)$$

By using the present method, the eigenvalue can be obtained by solving Eq.(50). The error curves of the first three non-zero eigenvalues with different numbers of sub-fields are shown in Fig.5. According to the results, the errors are reduced significantly with the increasing of the number of sub-fields. The present predictions are accurate to the 13th significant digit when 30 subfields are divided.

8.2.Eigenvalues of a reentrant corner in anisotropic material

Consider a reentrant corner of 90° in anisotropic material as illustrated in Fig.6, the material properties are given by $k_{11} = -1$, $k_{22} = -2$ and $k_{12} = 0.75$. The three typical types of boundary conditions as defined in Eqs.(10), (11) and (12) are investigated. For prescribed heat flux boundary condition, the eigenvalue is proven to satisfy the following governing equation [19], as specified by

$$\tan \left[\mu \left(\frac{\pi}{2} - \arctan \left(\frac{3}{\sqrt{23}} \right) \right) \right] + \tan(\mu\pi) = 0 \quad (64)$$

The analytical solution of eigenvalue can be obtained by solving this governing equation.

The error curves of the present numerical solution comparing with the analytical solution obtained by solving Eq.(64) are shown in Fig.7. According to the results shown in the figure, it is clear that the error decreases with the increasing of the sub-field number. However, the errors are larger than those for the crack problem with the same numbers of subfield as shown in Fig.5. The reason could be the angular distributions of heat fluxes are more complex than the crack problem discussed above, so more sub-fields are required. Nevertheless, the accuracy can be improved by using more sub-fields and the present predictions are accurate to 3rd significant digit with 180 subfields which is acceptable in engineering practice. The present solution of eigenvalue for all the boundary conditions are listed in Tab.1, extensive numerical results with enough numbers of significant digits are provided to the readers for possible comparison with their results.

8.3.GFIFs of the cracked disc of anisotropic material

Consider a cracked disc of anisotropic material of which the conductivity coefficients are specified by $k_{11} = -1$, $k_{22} = 0.75$ and $k_{12} = -2$. The radius of the disc is 2.0 as shown in Fig.8. Prescribed heat flux boundary condition as defined in Eq.(10) are considered on the crack surfaces. On the circumference of the disc, the temperature can be set according to

$$T = 2.123456\rho^{0.5}e^{\alpha\vartheta(\theta_i)}(A\cosh(\beta\vartheta(\theta_i)) + B\sinh(\beta\vartheta(\theta_i))) \quad (65)$$

Actually, the above equation is obtained from the eigen expansion Eq.(52) by setting the expanding coefficient $a^{(1)} = 2.123456$ and other expanding coefficients be zeroes. In Eq.(65), ρ is the radius and $\vartheta(\theta_i)$ is the local coordinate of the i th node of the SASE. For the first material the values of “ A ” and “ B ” are 1 and 0, respectively. However, for the other sub-fields, the values of “ A ” and “ B ” should be calculated through Eq.(45). It may be noted that Eq.(65) is defined in the local coordinate system and the coefficients α , β should be calculated separately for each sub-field. The exact solution of the GFIFs can be calculated directly through Eq.(59).

First, the results of the first 3 GFIFs corresponding to non-zero eigenvalues are calculated with different meshes (as shown in Fig.9) and listed in Tab.2. The other parameters are: 1000 sub-fields are divided, 50 Gaussian integration points are used in each sub-field, the radius of the SASE is 1.0, and 31 nodes are used in the SASE. All the parameters are chosen in the “finest” manner to reduce the negative influence on the numerical predictions. In the sub-figures (a), (b) and (c) of Fig.9, the disc is meshed with the SASE and regular elements, and in (d) it is meshed only by regular elements. The difference between (c) and (d) is that the SASE is replaced by 300 regular elements. In the case of (d), the nodal temperature is calculated by using regular elements and the GFIF is calculated by Eq.(59) although SASE is not used in the modelling. According to the results in Tab.2, it is interesting to find that the results obtained with the SASE are identical with each other, and all of them are very close to the exact solution. The reason could be the other parameters are too fine (especially for the number of sub-fields and the number of nodes in the SASE), and the influence of the mesh is very limited for this case. Hence, in the following calculations, the finest mesh which should be precise enough is adopted. However, the results obtained by using regular elements are not as accurate as those obtained with the SASE according to Tab.2. Although 300 more degree of freedoms are used in the modelling, the singularity problem in the crack tip area is still not treated properly, and this is the reason for the low solving accuracy and efficiency of regular element.

Next, the influence of the number of sub-fields is investigated. Keep the other parameters unchanged, the numerical results with different numbers of sub-fields are listed in Tab.3. It is easy to find that clear convergent results are obtained in Tab.3, the more sub-fields used, the higher the accuracy is. When 1000 sub-fields are used, the results become stable, and hence in the following calculations 1000 subfields are used. The angular distributions of ψ_r and ψ_s with 1000 sub-fields are shown in Fig.10 and Fig.11, respectively, it can be seen that both of the distributions are very smooth. In Tab.4, the present results with different nodes of the SASE are listed, it is concluded that more nodes used in the SASE can improve the solving accuracy. In Tab.5, the influence of the size of the SASE is investigated, it is concluded that the size of the SASE doesn't have a strong influence on the numerical results. It means that the present method is very robust and stable. In Tab.6, the influence of the number of Gaussian integration points is investigated. It is found that the solution with only 1 Gaussian integration point in each subfield is already accurate. The reason is that there are 1000 sub-fields in the domain and each sub-field is very small, and hence the number of Gaussian point doesn't have a strong influence. When the GFIFs are obtained, the values of heat fluxes can be obtained, the contours of q_x and q_y in the SASE are shown in Fig.12.

8.4.GFIFs of an edge crack in anisotropic material

Consider an edge crack problem as shown in Fig.13, the crack length is 4 mm and W is 10 mm. The conductivity coefficients are specified by $k_{11} = -1$, $k_{22} = 0.75$ and $k_{12} = -2$. The left and right sides of the rectangular plate as well as the crack surfaces are insulated, the temperature at the lower side of the plate is prescribed by $T_2=100$ °C. In the modelling, 31 nodes are used in the SASE, and the radius of the SASE is 2 mm. A total of 1000 sub-fields are divided and 3 Gaussian integration points are used in each sub-field. Two mesh strategies are used as shown in Fig.13, one is meshed with the SASE while the other one is meshed purely by using regular elements. The GFIFs with different temperatures T_1 at the upper side of the plate obtained by using the SASE are listed in Tab.7. When $T_1=0$, the results obtained by using regular elements are also listed in the table. It is seen that when 900 regular elements are used to mesh the crack tip area the numerical predictions are close to those obtained by using only one SASE, indicating that the solving accuracy of the proposed SASE is much higher. The contours of temperature and heat fluxes in the cracked plate when $T_2=160$ °C are shown in Fig.14 and Fig.15,

respectively. Due to material anisotropy, the contour lines of temperature have an orientation and the values of q_x are not zero in the area. The temperature is smooth in the most of the structure except on the crack where it is interrupted and a temperature jump is resulted in. The detailed contours of the heat fluxes around the crack tip are also provided. According to the contours of the heat fluxes, it is found that the magnitude of heat fluxes are stable and small in the most area of the plate except the crack tip area. The detailed contours around the crack tip are provided with finer levels, the absolute values of the heat fluxes increase smoothly in the area indicating that the singularities of both heat fluxes have been predicted very well.

8.5.GFIFs of a reentrant corner in anisotropic material

Consider a plate with a reentrant corner of 90° as shown in Fig.16, the insulated sides of the plate are marked in the figure by $q_x = 0$ or $q_y = 0$ depending on the orientation of the side. The conductivity coefficients are specified by $k_{11} = -1$, $k_{22} = 0.75$ and $k_{12} = -2$. The geometric parameter is $W = 5\text{mm}$. The left side of the plate is constrained by prescribed temperature $T_1 = 100^\circ\text{C}$. In the modelling, 21 nodes of the SASE are used and the radius of the SASE is 2 mm. 750 sub-fields are used and 3 Gaussian points are used in each sub-field. These parameters are chosen based on the opening angle of the structure. Two mesh strategies are shown in Fig.16, one is meshed with the SASE while the other one is meshed purely by using regular elements. Numerical results of the GFIFs with different temperatures T_2 on the right side of the plate obtained by using the SASE are listed in Tab.8. When $T_1=0$, the results obtained by using regular elements are also listed in the table. Again, it is demonstrated that the solving efficiency of the proposed SASE is much higher than regular element. The contours of temperature and heat fluxes are shown in Fig.17 and Fig.18, respectively. According to the results, the prescribed boundary conditions of temperature as well as heat fluxes are satisfied very well. The heat flux singularities have been well predicted.

9.Conclusions

The steady-state thermal conduction with singularity due to the existence of v-notch or crack in anisotropic material is studied both analytically and numerically. In order to overcome the bottleneck of the symplectic dual approach for anisotropic material under the polar coordinate system, a sub-field method is introduced to divide the material into several sub-fields, assuming the equivalent conductivity coefficients in each sub-field be constants. As such, the original problem has been solved analytically

and the symplectic eigen solutions are obtained for the first time. Based on the eigen solution, a symplectic analytical singular element (SASE) is constructed for the numerical study of the structure with complex geometry, loading condition or constrain types; as a result, the generalized flux intensity factors (GFIFs) can be solved directly without any post-processing. A few numerical examples have been worked out to demonstrate the proposed method. It is proven that both of the eigen solution and the GFIFs obtained by the proposed methods are close to the exact solutions if sufficient numbers of sub-field are used. According to the numerical results, it is found that 1000 sub-field for a crack and 750 sub-fields for a reentrant corner of 90° are sufficient enough for satisfactory numerical results. Besides, the basic features of the proposed SASE have been checked and a few conclusions can be made: (1) more nodes of the SASE can improve the solving accuracy significantly, (2) The number of Gaussian integration points (GIPs) in each sub-field does not have a strong effect on the numerical results when 1000 or more sub-fields are used while 3 GIPs for each sub-field are enough, and (3) the numerical predictions are very accurate under a large range of sizes of the SASE, hence the empirical knowledge on choosing proper element size is not required. The proposed method can be extended to the case of multiple anisotropic materials, which will be addressed in future publications.

10. Acknowledgements

The support of the National Natural Science Foundation of China (No.11502045) is gratefully acknowledged.

References

- [1]. Ma CC, Chang SW. Analytical exact solutions of heat conduction problems for anisotropic multi-layered media. *International Journal of Heat and Mass Transfer*, 2004, 47: 1643-1655.
- [2]. Tsai TW, Lee YM, Shiah YC. Heat Conduction Analysis in an Anisotropic Thin Film Irradiated by an Ultrafast Pulse Laser Heating. *Numerical Heat Transfer, Part A: Applications*, 2013, 64: 132-152.
- [3]. Chen T, Kuo HY. On linking n-dimensional anisotropic and isotropic Green's functions for infinite space, half-space, bimaterial, and multilayer for conduction. *International Journal of Solids and Structures*, 2005, 42: 4099-4114.
- [4]. Yen DHY, Beck JV. Green's functions and three-dimensional steady-state heat-conduction problems in a two-layered composite. *Journal of Engineering Mathematics*, 2004, 49: 305-319.
- [5]. Marczak RJ, Denda M. New derivations of the fundamental solution for heat conduction problems in three-dimensional general anisotropic media. *International Journal of Heat and Mass Transfer*, 2011, 54: 3605-3612.

-
- [6]. Shiah YC, Hwang PW, Yang RB. Heat conduction in multiply adjoined anisotropic media with embedded point heat sources. *Journal of Heat Transfer*, 2006, 128: 207-214.
- [7]. Rafiezadeh K, Ataie-Ashtiani B. Seepage analysis in multi-domain general anisotropic media by three-dimensional boundary elements. *Engineering Analysis with Boundary Elements*, 2013, 37: 527-541.
- [8]. Marin L, Munteanu L. Boundary reconstruction in two-dimensional steady state anisotropic heat conduction using a regularized meshless method. *International Journal of Heat and Mass Transfer*, 2010, 53: 5815-5826.
- [9]. Zhang YM, Liu ZY, Chen JT, Gu Y. A novel boundary element approach for solving the anisotropic potential problems. *Engineering Analysis with Boundary Elements*, 2011, 35: 1181-1189.
- [10]. Gu Y, Chen W, He XQ. Singular boundary method for steady-state heat conduction in three dimensional general anisotropic media. *International Journal of Heat and Mass Transfer*, 2012, 55: 4837-4848.
- [11]. Yeh CS, Shu YC, Wu KC. Conservation laws in anisotropic elasticity II. Extension and application to thermoelasticity, *Proceedings of the Royal Society A*, 1993, 443, 39–151.
- [12]. Kattis MA, Papanikos P, Providas E. Thermal Green's functions in plane anisotropic bimetals, *Acta Mechanica*. 2004, 173, 65–76.
- [13]. Sladek J, Sladek V, Hellmich Ch, Eberhardsteiner J. Heat conduction analysis of 3-D axisymmetric and anisotropic FGM bodies by meshless local Petrov–Galerkin method. *Computational Mechanics*, 2007, 39: 323-333.
- [14]. Buroni FC, Marczak RJ, Denda M, Saez A. A formalism for anisotropic heat transfer phenomena: Foundations and Green's functions. *International Journal of Heat and Mass Transfer*, 2014, 75: 399-409.
- [15]. Berger JR, Martin PA, Mantič V, Gray LJ. Fundamental solutions for steady-state heat transfer in an exponentially graded anisotropic material. *Zeitschrift für Angewandte Mathematik und Physik (ZAMP)*, 2005, 56: 293-303.
- [16]. Shen MH, Chen FM, Hung SY. Analytical solutions for anisotropic heat conduction problems in a trimaterial with heat sources. *Journal of Heat Transfer*, 2010, 132: 091302.
- [17]. Hu XF, Gao HY, Yao WA, Yang ST. Study on steady-state thermal conduction with singularities in multi-material composites. *International Journal of Heat and Mass Transfer*, 2017, 104: 861-870.
- [18]. Hu XF, Gao HY, Yao WA, Yang ST. A symplectic analytical singular element for steady-state thermal conduction with singularities in composite structures. *Numerical Heat Transfer, Part B: Fundamentals*, 2016, 70: 406-419.
- [19]. Yosibash Z. *Singularities in elliptic boundary value problems and elasticity and their connection with failure initiation*. Springer, New York, 2011.
- [20]. Mantič V, Paris F, Berger J. Singularities in 2D anisotropic potential problems in multi-material corners: Real variable approach. *International Journal of Solids and Structures*, 2003, 40: 5197-5218.
- [21]. Hwu C, Lee WJ. Thermal effect on the singular behavior of multibonded anisotropic wedges. *Journal of Thermal Stresses*, 2004, 27: 111-136.
- [22]. Chao CK, Chang RC. Thermal interface crack problems in dissimilar anisotropic media. *Journal of Applied Physics*, 1992, 72: 2598-2604.
- [23]. Yu TT, Bui TQ, Yin SH, Doan DH, Wu CT, Do TV, Tanaka S, On the thermal buckling analysis of functionally graded plates with internal defects using extended isogeometric analysis. *Composite Structures*, 2016, 136: 684-695.

-
- [24]. Liu P, Yu T, Bui TQ, Zhang CZ, Xu YP, Lim CW. Transient thermal shock fracture analysis of functionally graded piezoelectric materials by the extended finite element method. *International Journal of Solids and Structures*, 2014, 51: 2167-2182.
- [25]. Tanaka S, Suzuki H, Sadamoto S, Imachi M, Bui TQ. Analysis of cracked shear deformable plates by an effective meshfree plate formulation. *Engineering Fracture Mechanics*, 2015, 144: 142-157.
- [26]. Lei J, Zhang CZ, Bui TQ. Transient dynamic interface crack analysis in magneto-electroelastic bi-materials by a time-domain BEM. *European Journal of Mechanics-A/Solids*, 2015, 49: 146-157.
- [27]. Hosseini SS, Bayesteh H, Mohammadi S. Thermo-mechanical XFEM crack propagation analysis of functionally graded materials. *Materials Science and Engineering: A*, 2013, 561: 285-302.
- [28]. Yvonnet J, He QC, Zhu QZ, Shao JF. A general and efficient computational procedure for modelling the Kapitza thermal resistance based on XFEM. *Computational Materials Science*. 2011, 50: 1220-1224.
- [29]. Marin L. A meshless method for the stable solution of singular inverse problems for two-dimensional Helmholtz-type equations. *Engineering Analysis with Boundary Elements*, 2010, 34: 274-288.
- [30]. Marin L. Treatment of singularities in the method of fundamental solutions for two-dimensional Helmholtz-type equations. *Applied Mathematical Modelling*, 2010, 34: 1615-1633.
- [31]. Marin L, Lesnic D, Mantič V. Treatment of singularities in Helmholtz-type equations using the boundary element method. *Journal of Sound and Vibration*, 2004, 278: 39-62.
- [32]. Mera NS, Elliott L, Ingham DB, Lesnic D. Singularities in anisotropic steady - state heat conduction using a boundary element method. *International Journal for Numerical Methods in Engineering*, 2002, 53: 2413-2427.
- [33]. Mera NS, Elliott L, Ingham DB, Lesnic D. An iterative algorithm for singular Cauchy problems for the steady state anisotropic heat conduction equation. *Engineering Analysis with Boundary Elements*, 2002, 26: 157-168.
- [34]. Gu Y, Chen W, Fu ZJ. Singular boundary method for inverse heat conduction problems in general anisotropic media. *Inverse Problems in Science and Engineering*, 2014, 22: 889-909.
- [35]. Wei X, Chen W, Chen B, Sun L. Singular boundary method for heat conduction problems with certain spatially varying conductivity. *Computers & Mathematics with Applications*, 2015, 69: 206-222.
- [36]. Mierzwiczak M, Chen W, Fu ZJ. The singular boundary method for steady-state nonlinear heat conduction problem with temperature-dependent thermal conductivity. *International Journal of Heat and Mass Transfer*, 2015, 91: 205-217.
- [37]. Shannon S, Yosibash Z, Dauge M, Costabel M. Extracting generalized edge flux intensity functions with the quasilocal function method along circular 3-D edges, *International Journal of Fracture*, 2013, 181:25–50.
- [38]. Xiao QZ, Karihaloo BL. Improving the accuracy of XFEM crack tip fields using higher order quadrature and statically admissible stress recovery. *International Journal for Numerical Methods in Engineering*, 2006, 66: 1378-1410.
- [39]. Leung AYT, Xu XS, Zhou ZH. Hamiltonian approach to analytical thermal stress intensity factors-Part 1: Thermal Intensity Factor. *Journal of Thermal Stresses*, 2010, 33: 262-278.
- [40]. Zhou ZH, Xu CH, Xu XS, Leung AYT. Finite-element discretized symplectic method for steady-state heat conduction with singularities in composite structures. *Numerical Heat Transfer, Part B: Fundamentals*, 2015, 67: 302-319.
- [41]. Lim CW, Xu XS. Symplectic elasticity: theory and applications. *Applied Mechanics Reviews*, 2010, 63: 050802.

-
- [42]. Li J. Singularity analysis of near-tip fields for notches formed from several anisotropic plates under bending. *International Journal of Solids and Structures*, 2002, 39: 5767-5785.
- [43]. Li J, Zhang XB, Recho N. Stress singularities near the tip of a two-dimensional notch formed from several elastic anisotropic materials. *International Journal of Fracture*, 2001, 107: 379-395.
- [44]. Hu XF, Yao WA, Fang ZX. Stress singularity analysis of anisotropic multi-material wedges under antiplane shear deformation using the symplectic approach. *Theoretical and Applied Mechanics Letters*, 2011, 1, 061003.
- [45]. Hahn DW and Özişik MN. *Heat Conduction*, Third Edition, John Wiley & Sons, Inc., Hoboken, NJ, USA, 2012.

Captions of figures and tables

Fig.1 A wedge in anisotropic material and the sub fields

Fig.2 Schematic illustration of a sub-field.

Fig.3 The symplectic analytical singular element

Fig.4 The flow chat of the proposed method for wedge problem in anisotropic material

Fig.5 Error curves of the eigenvalue for a crack

Fig.6 Schematic of a reentrant corner of 90°

Fig.7 Curves of error of the present solution of eigenvalue for a reentrant

Fig.8 A cracked disc of anisotropic material

Fig.9 The FE meshes of the cracked disc with a SASE and a few four node isoparametric elements.

There are 60, 180, and 300 four node elements in the coarse mesh, middle mesh and refined mesh, respectively.

Fig.10 The angular distribution of ψ_r from the first five eigenvectors (non-zero)

Fig.11 The angular distribution of ψ_s from calculated the first five eigenvectors (non-zero)

Fig.12 Contours of q_x and q_y in the SASE

Fig.13 An edge crack in the plate of anisotropic material and the FE mesh

Fig.14 Contours of temperature in the cracked plate

Fig.15 Contours of heat fluxes in the cracked plate

Fig.16 Configuration of a reentrant corner of 90° and the FE mesh

Fig.17 Contours of temperature in the plate with a reentrant

Fig.18 Contours of heat fluxes in the plate with a reentrant

Tab.1 Nonzero eigenvalues of a reentrant corner in anisotropic material. The boundary condition (B.C.)

#1 is prescribed heat flux at both of the surfaces, B.C. #2 is prescribed heat flux at surface #1 and prescribed heat flux at surface #2, B.C. #3 is prescribed temperature at both surfaces of the reentrant corner.

Tab.2 Numerical predictions with different mesh and the exact solutions of the first few GFIFs.

Tab.3 Numerical predictions with different numbers of sub-field

Tab.4 Numerical predictions with different numbers of nodes of the SASE

Tab.5 Numerical predictions with different sizes of the SASE

Tab.6 Numerical predictions with different numbers of Gaussian integration points

Tab.7 Numerical predictions of GFIFs for an edge crack in anisotropic material

Tab.8 Numerical predictions of GFIFs for a reentrant in anisotropic material

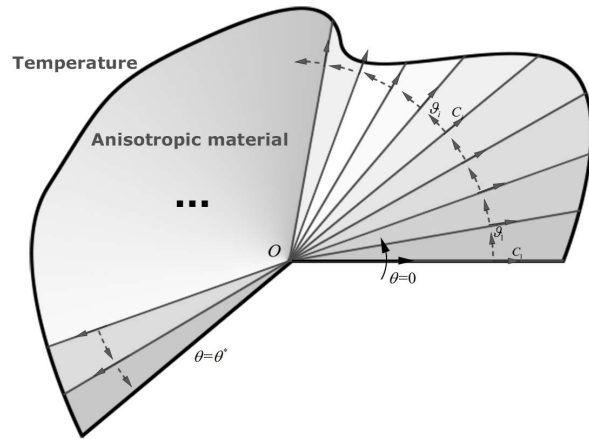


Fig.1 A wedge in anisotropic material and the sub fields

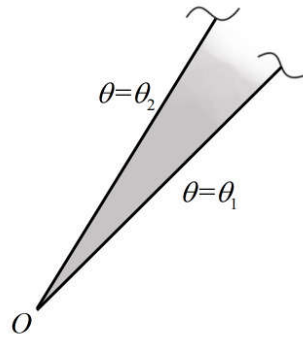


Fig.2. Schematic illustration of a sub-field.

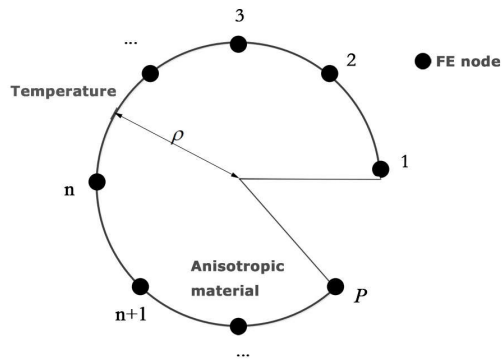


Fig.3. The symplectic analytical singular element

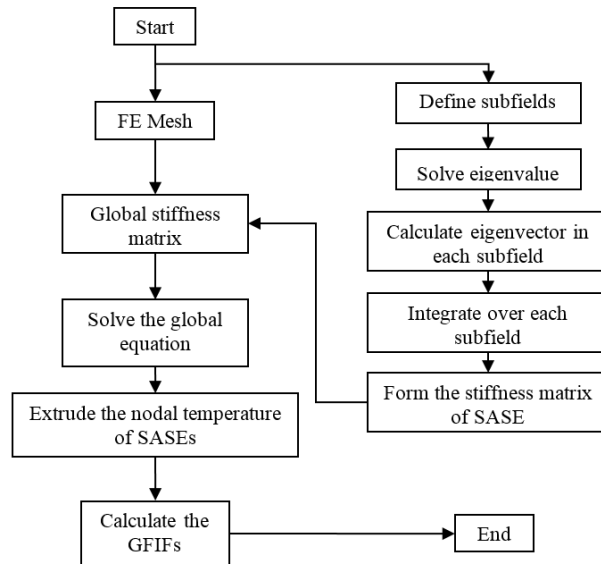


Fig.4. The flow chat of the proposed method for wedge problem in anisotropic material

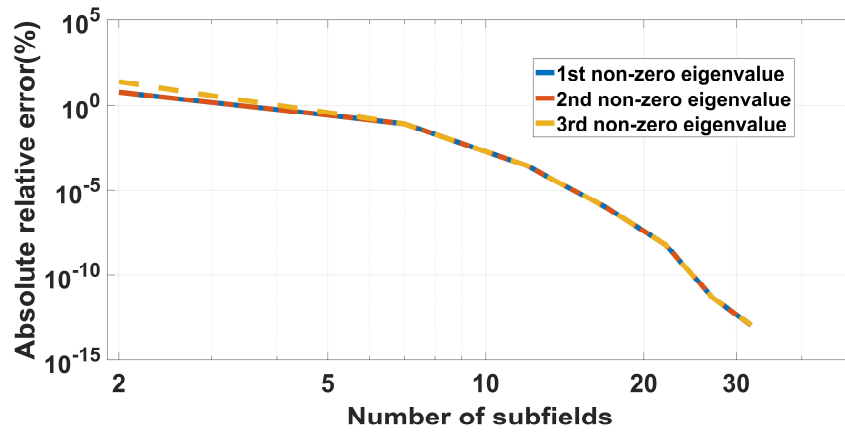


Fig.5. Error curves of the eigenvalue for a crack

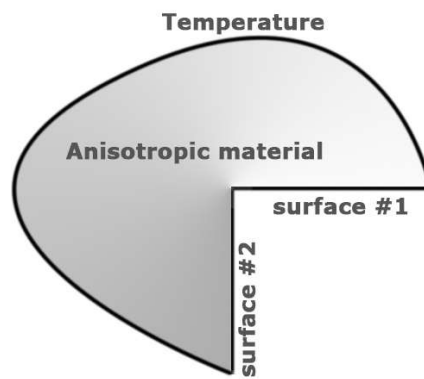


Fig.6. Schematic of a reentrant corner of 90°

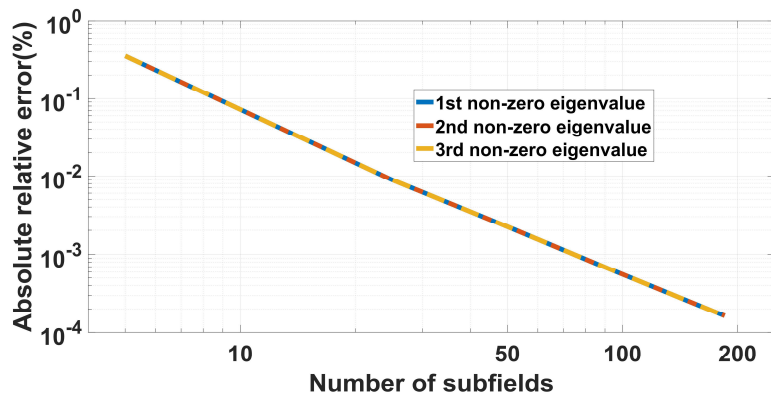


Fig.7. Curves of error of the present solution of eigenvalue for a reentrant

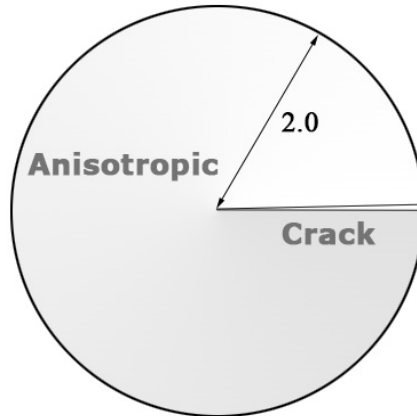


Fig.8. A cracked disc of anisotropic material

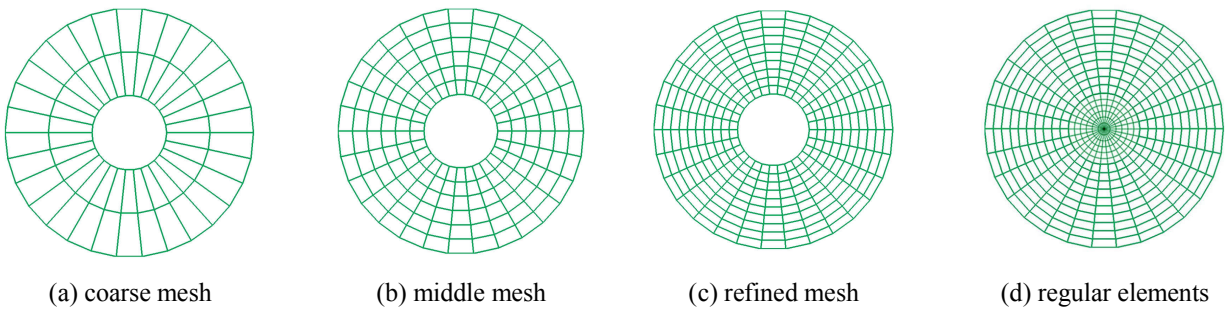


Fig.9. The FE meshes of the cracked disc with a SASE and a few four node isoparametric elements. There are 60, 180, and 300 four node elements in the coarse mesh, middle mesh and refined mesh, respectively. In the sub-figure (d), the disc is meshed only by using regular elements.

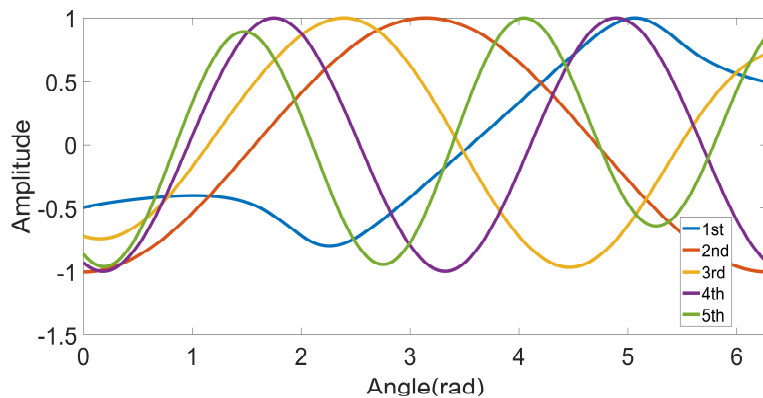


Fig.10. The angular distribution of ψ_r from the first five eigenvectors (non-zero)

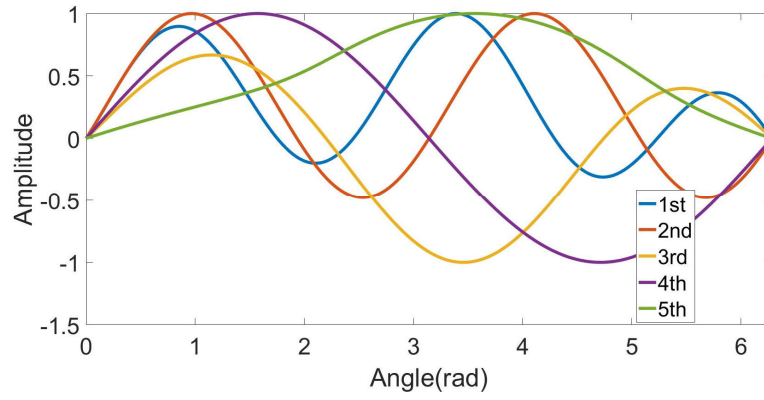


Fig.11. The angular distribution of ψ_s from calculated the first five eigenvectors (non-zero)

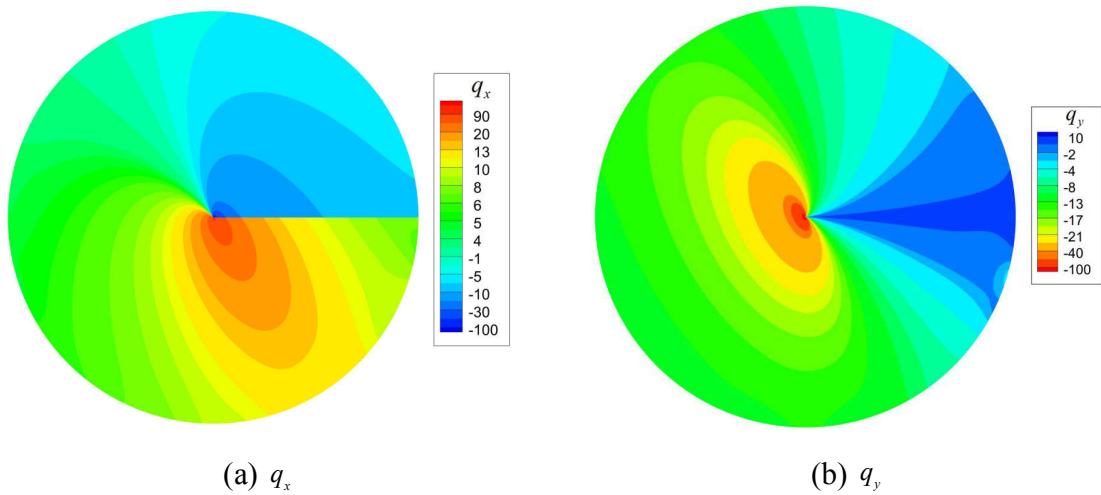


Fig.12. Contours of q_x and q_y in the SASE

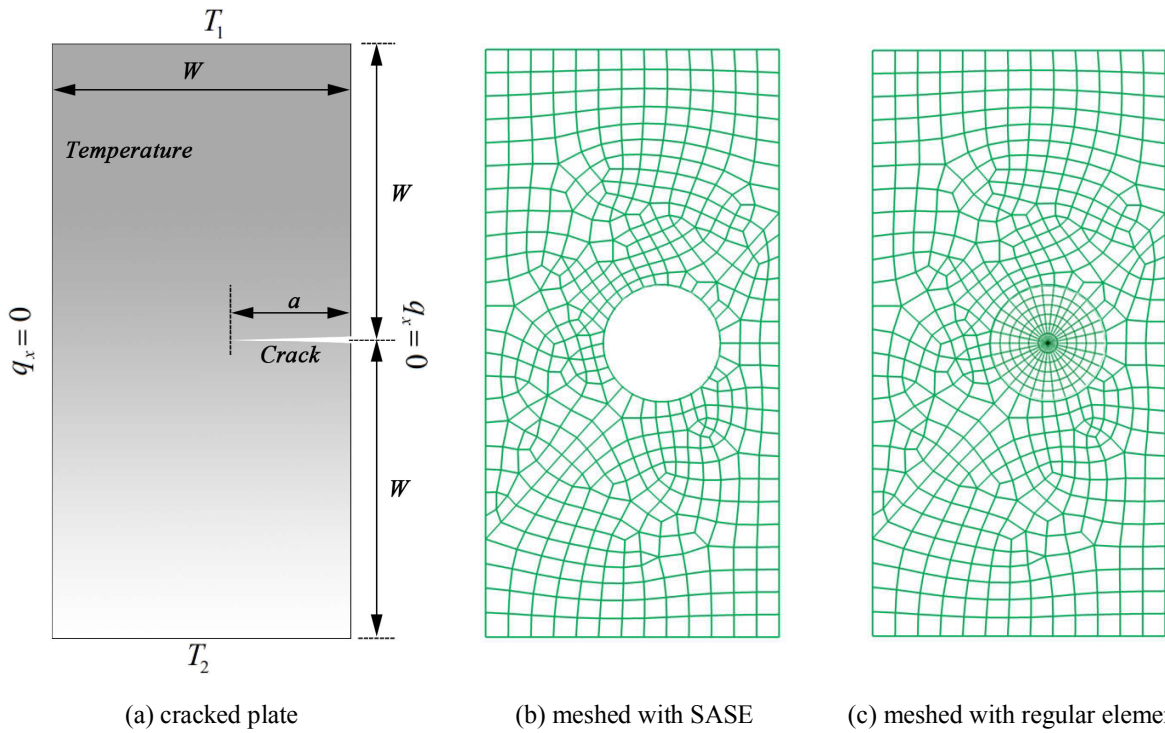


Fig.13. An edge crack in the plate of anisotropic material and the FE mesh. In the sub-figure (b), the crack tip area is meshed by using a SASE while in (c) the whole structure is meshed by using regular elements, the SASE is replaced by 300 regular elements.

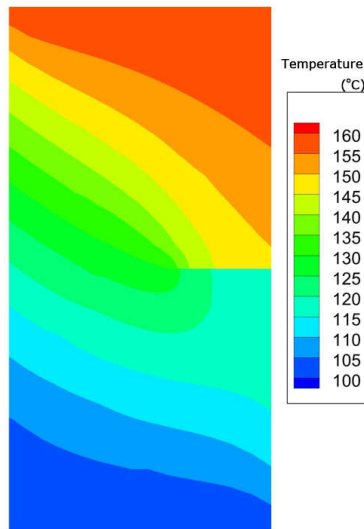


Fig.14. Contours of temperature in the cracked plate

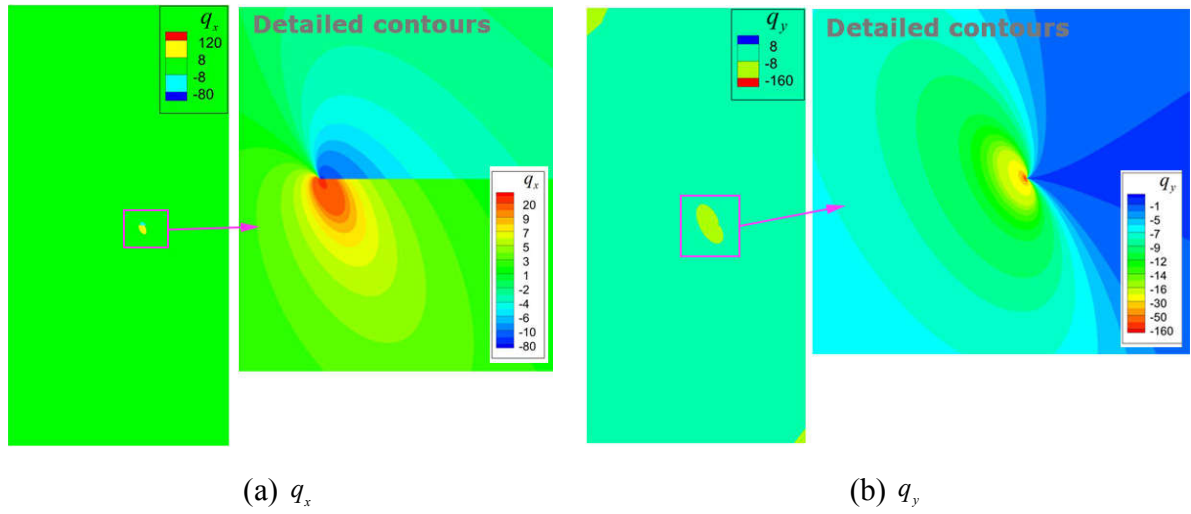


Fig.15. Contours of heat fluxes in the cracked plate

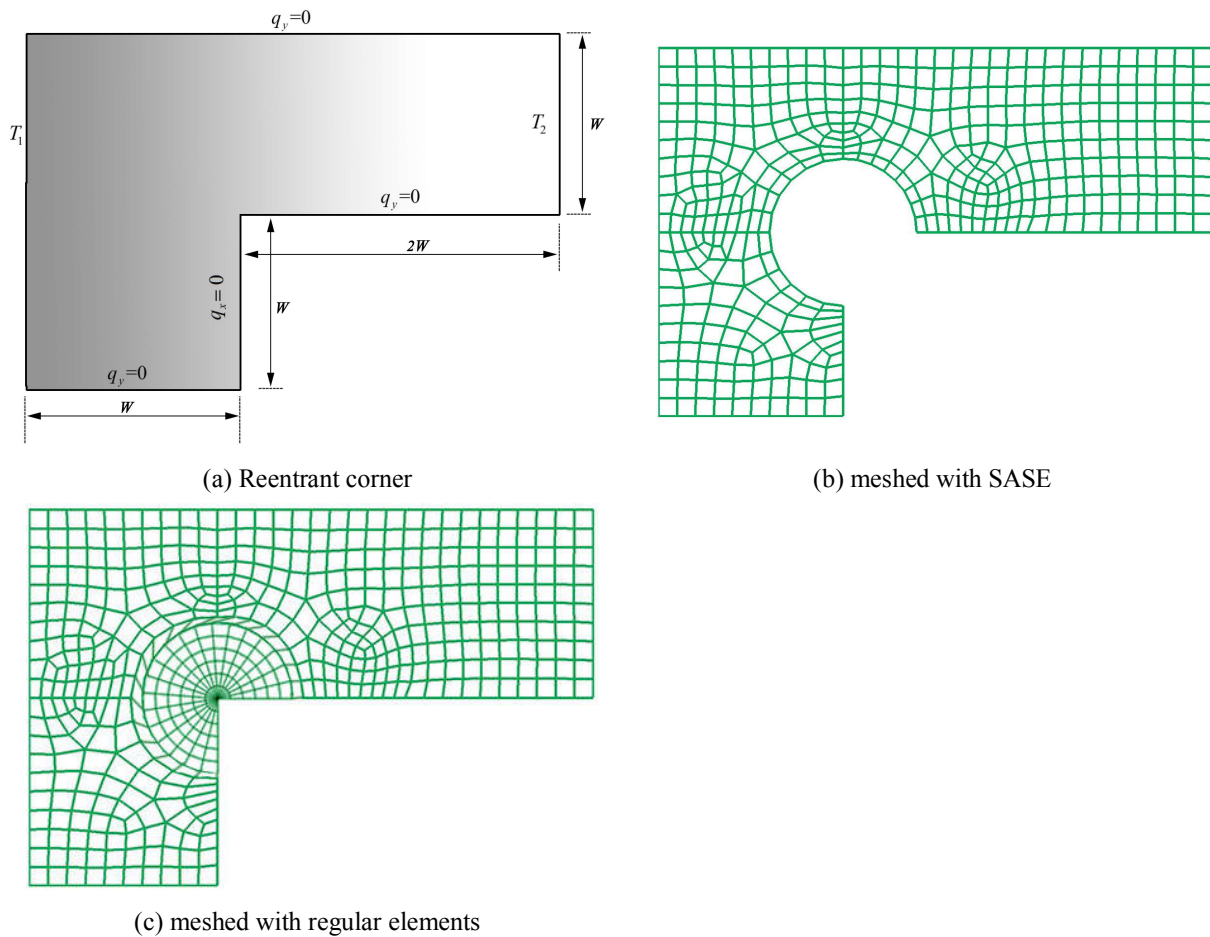


Fig.16. Configuration of a reentrant corner of 90° and the FE mesh. In the sub-figure (b), the corner area is meshed by a SASE while in (c) the whole structure is meshed by regular elements.

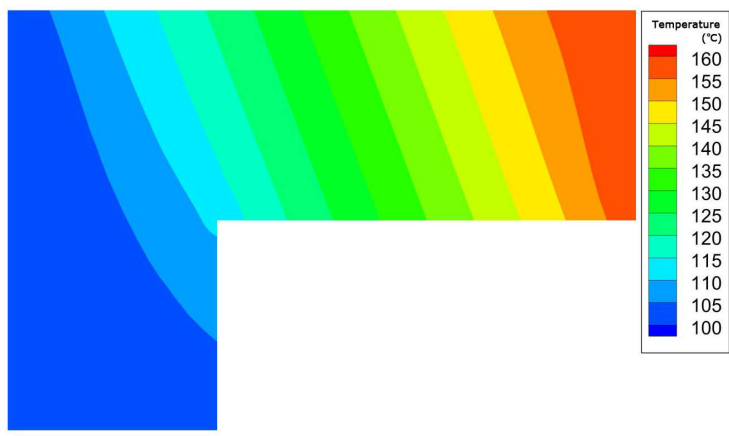


Fig.17. Contours of temperature in the plate with a reentrant

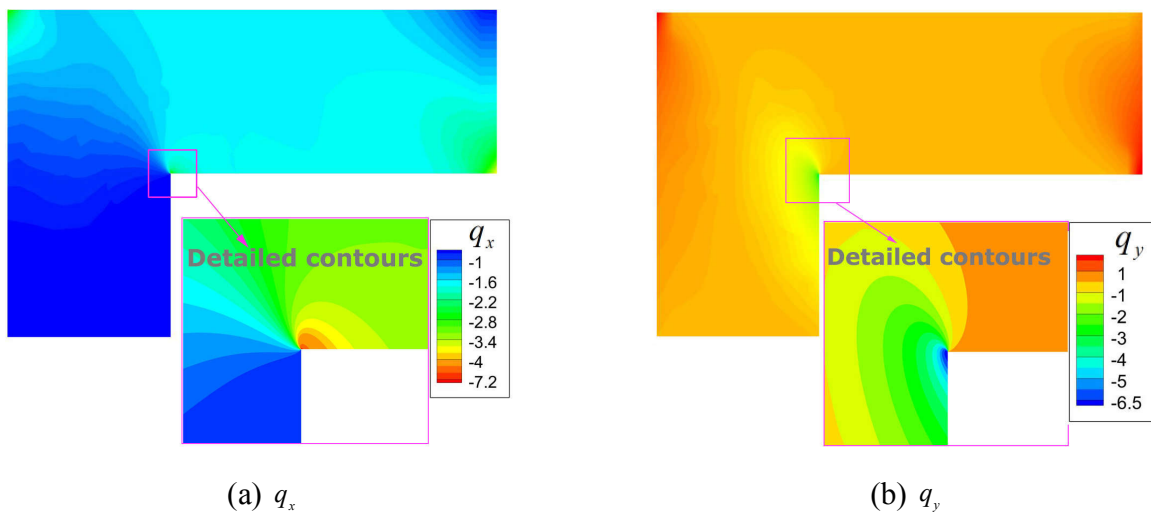


Fig.18. Contours of heat fluxes in the plate with a reentrant

Tab.1 Nonzero eigenvalues of a reentrant corner in anisotropic material. The boundary condition (B.C.) #1 is prescribed heat flux at both of the surfaces, B.C. #2 is prescribed heat flux at surface #1 and prescribed heat flux at surface #2, B.C. #3 is prescribed temperature at both surfaces of the reentrant corner.

		1	2	3	4	5
B.C. #1	Present	0.756393	1.512787	2.269181	3.025575	3.781968
	Analytical [19]	0.756391	1.512781	2.269172	3.025563	3.781954
	Error %	0.000386	0.000386	0.000386	0.000386	0.000386
B.C. #2	Present	0.378197	1.134592	1.890987	2.647382	3.403777
B.C. #3	Present	0.756395	1.512790	2.269185	3.025580	3.781975

Tab.2 Numerical predictions with different mesh and the exact solutions of the first few GFIFs.

Mesh	1st	2nd	3rd
Coarse mesh	2.123869	0.002050	0.000475
Middle mesh	2.123869	0.002050	0.000475
Refined mesh	2.123869	0.002050	0.000475
300 regular elements	2.054616	0.004315	0.006476
Exact solution	2.123456	0	0

Tab.3 Numerical predictions with different numbers of sub-field

Numb. sub-fields	1st	2nd	3rd
50	2.138074	0.027404	-0.057741
100	2.128103	0.016220	-0.020810
500	2.124115	0.003812	-0.001291
1000	2.123869	0.002050	0.000475
2000	2.123772	0.001151	0.001293
4000	2.123728	0.000697	0.001687
Exact solution	2.123456	0	0

Tab.4 Numerical predictions with different numbers of nodes of the SASE

Num. export nodes	1st	2nd	3rd
11	2.125390	-0.001083	0.008491
16	2.124446	0.002231	0.016542
21	2.124060	0.002517	0.003667
26	2.123992	0.002055	0.002077
31	2.123869	0.002050	0.000475
Exact solution	2.123456	0	0

Tab.5 Numerical predictions with different sizes of the SASE

ρ	1st	2nd	3rd
0.2	2.140670	-0.000945	-0.013892
0.6	2.125284	0.002437	0.001884
1.0	2.123869	0.002050	0.000475
1.4	2.123445	0.001371	-0.000098
1.8	2.123326	0.000506	-0.000194
Exact solution	2.123456	0	0

Tab.6 Numerical predictions with different numbers of Gaussian integration points

Number of G.P.	1st	2nd	3rd
1	2.123868	0.002052	0.000493
3	2.123869	0.002050	0.000475
5	2.123869	0.002050	0.000475
10	2.123869	0.002050	0.000475
20	2.123869	0.002050	0.000475
50	2.123869	0.002050	0.000475
Exact solution	2.123456	0	0

Tab.7 Numerical predictions of GFIFs for an edge crack in anisotropic material

$T_1(^{\circ}C)$	1st	2nd	3rd
0	-2.416560	-0.657906	0.495092
0 (300 regular elements)	-2.321313	-0.611241	0.432170
0 (600 regular elements)	-2.428563	-0.614564	0.438343
0 (900 regular elements)	-2.410978	-0.623423	0.451241
20	-1.933248	-0.526325	0.396073
40	-1.449936	-0.394744	0.297055
60	-0.966624	-0.263163	0.198037
80	-0.483312	-0.131581	0.099018
100	0.000000	0.000000	0.000000
120	0.483312	0.131581	-0.099018
140	0.966624	0.263163	-0.198037
160	1.449936	0.394744	-0.297055

Tab.8 Numerical predictions of GFIFs for a reentrant in anisotropic material

$T_2(^{\circ}C)$	1st	2nd	3rd
0	3.314970	0.944047	-0.059913
0 (200 regular elements)	3.257012	0.838749	-0.125123
0 (600 regular elements)	3.321231	0.890437	-0.025846
20	2.651976	0.755237	-0.047930
40	1.988982	0.566428	-0.035948
60	1.325988	0.377619	-0.023965
80	0.662994	0.188809	-0.011983
100	0.000000	0.000000	0.000000
120	-0.662994	-0.188809	0.011983
140	-1.325988	-0.377619	0.023965
160	-1.988982	-0.566428	0.035948